Fuel 324 (2022) 124822

Contents lists available at ScienceDirect

Fuel

journal homepage: www.elsevier.com/locate/fuel

Full Length Article

Carbon nanotube supported Ga@PdAgCo anode catalysts for hydrazine electrooxidation in alkaline media

Sefika Kaya [a,*], Aykut Caglar [a,b], Hilal Kivrak [a,c,d,*]

[a] Department of Chemical Engineering, Faculty of Engineering and Architectural Sciences, Eskisehir Osmangazi University, Eskisehir 26040, Turkey
[b] Department of Chemical Engineering, Faculty of Engineering, Van Yüzüncü Yil University, Van 65000, Turkey
[c] Translational Medicine Research and Clinical Center, Eskisehir Osmangazi University, 26040 Eskisehir, Turkey
[d] Kyrgyz-Turk Manas University, Faculty of Engineering, Department of Chemical Engineering, Bishkek, Kyrgyzstan, Turkey

ARTICLE INFO

Keywords:
Ga
Pd
Ag
Co
Carbon nanotube
Hydrazine electrooxidation

ABSTRACT

In this study, carbon nanotube supported (CNT) monometallic (Pd), trimetallic (PdAgCo), and multimetallic (Ga@PdAgCo) catalysts in different weight percentages (0.5–10%) are synthesized by the $NaBH_4$ reduction method and characterized transmission electron microscopy (TEM), X-ray photoelectron spectroscopy (XPS), inductively coupled plasma-mass spectrometry (ICP-MS), and X-ray diffraction (XRD) analytical methods. According to the TEM analysis results, while agglomeration doesn't observe for 3% Ga@PdAgCo(80:10:10)/CNT catalyst, agglomeration is observed in certain parts for 7% Ga@PdAgCo(80:10:10)/CNT catalyst. The occurrence of agglomeration has a negative effect on catalytic activity. XRD analysis shows that as metal was added, the diffraction peaks are negatively shifted, thereby forming an alloy. Electrochemical measurements such as cyclic voltammetry (CV), chronoamperometry (CA), and electrochemical impedance spectroscopy (EIS) are used for the hydrazine electrooxidation activities of the catalysts. The highest specific activity is achieved as 250.39 mA/cm^2 (22592.66 mA/mg Pd) with catalyst. The electrochemical surface area (ECSA) of 3% Ga@PdAgCo/CNT catalysts is also calculated as 1392.43 m^2/g. The homogeneous distribution of the metals on the support material and the alloy formation has an effect on the catalytic activity for the 3% Ga@PdAgCo(80:10:10)/CNT catalyst. Although Pd is an active metal on its own, the synergistic effect between them as a result of the formation of alloys with different metals and the electronic state change on the catalyst by adding different metals to Pd has a great influence on the catalytic activity. As a result, Ga@PdAgCo/CNT catalyst with its high current value stands out as a new anode catalyst for hydrazine electrooxidation.

1. Introduction

In recent years, alternative energy sources have gained importance in the face of increasing energy demand with population growth and industrialization [1,2]. Providing energy demand from fossil fuels such as coal, natural gas, and oil causes global warming and environmental pollution with the effect of greenhouse gasses [3,4]. The negative effects of fossil fuels on human health and environmental pollution have increased research on alternative energy sources such as solar energy, wind energy, nuclear energy, geothermal energy, and fuel cells [5,6]. Fuel cells have attracted attention in recent years with their low emissions and high energy efficiency [7-9].

Hydrazine (N_2H_4) has been preferred as a liquid fuel in fuel cell technology with its advantages such as safe storage and easy transportation [10]. Hydrazine is also non-explosive and can be stored in liquid form ($N_2H_4{\cdot}H_2O$) [11]. Hydrazine is toxic in its pure form, but its toxicity reduces in its liquid form [12-15]. Direct hydrazine fuel cells (DHFCs) have high energy density (5.4 kWh/L), fast reaction kinetics, and high theoretical cell voltage (1.56 V) [16-19]. In DHFCs, hydrazine electrooxidation does not produce CO_2, which pollutes the environment. Therefore, it is an environmentally friendly technology that does not cause greenhouse gas emissions [20-22]. The anode, cathode, and overall reaction of hydrazine electrooxidation are as follows [23,24]:

Anode reaction: $N_2H_4 + 4OH^- \rightarrow N_2 + 4H_2O + 4e^-$ (1)

Cathode reaction: $O_2 + 2H_2O + 4e^- \rightarrow 4OH^-$ (2)

* Corresponding author at: Department of Chemical Engineering, Faculty of Engineering and Architectural Sciences, Eskisehir Osmangazi University, Eskisehir 26040, Turkey (H. Kivrak).
E-mail addresses: sefikakaya@ogu.edu.tr (S. Kaya), hilaldemir.kivrak@ogu.edu.tr (H. Kivrak).

https://doi.org/10.1016/j.fuel.2022.124822
Received 3 April 2022; Received in revised form 2 June 2022; Accepted 5 June 2022
Available online 10 June 2022

Table 1
Onset potential and maximum current density values for hydrazine electrooxidation in literature.

Catalyst	OnsetPotential (V)	Reference Electrode	Current density (mA/cm^2)	Reference
VGNH-45	−0.42	SCE	13.0	[34]
AuPd dendritic alloyed nanocrystals	−0.11	SCE	9.57	[35]
MnO/N-C	−0.51	Hg/HgO	6.30	[36]
N-C	−0.43		2.52	
MnO	−0.415		0.20	
CPE/PpDP/ZnO	−0.06	Ag/AgCl	7.89	[37]
Co@NM	−0.16	Hg/HgO	8.13	[38]
NPGL30	–	SCE	10.5	[39]
NCS	0.38	SCE	2.88	[40]
SeNCM-800	0.43	RHE	15.6	[41]
SeNCM-900	0.40		22.3	
SeNCM-1000	0.34		30.8	
3%Ga@PdAgCo/CNT	−0.79	Ag/AgCl	250.39	This work

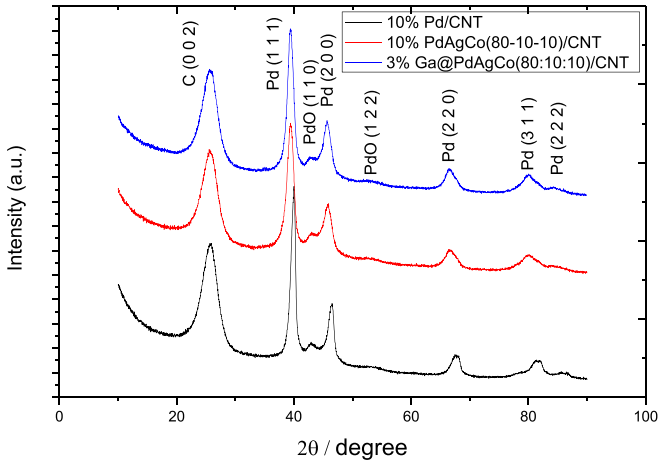

Fig. 1. XRD patterns of 10% Pd/CNT, 10% PdAgCo(80–10-10)/CNT, and 3% Ga@PdAgCo(80:10:10)/CNT catalysts.

Table 2
Diffraction peaks of XRD patterns at 2θ for 10% Pd/CNT, 10% PdAgCo(80–10-10)/CNT, and 3% Ga@PdAgCo(80:10:10)/CNT catalysts.

	Observed (degree)		
(*hkl*) planes	10% Pd/CNT	10% PdAgCo(80–10-10)/CNT	3% Ga@PdAgCo (80:10:10)/CNT
(111)	40.02	39.46	39.40
(110)	42.94	40.01	42.70
(200)	46.53	45.85	45.60
(122)	53.20	52.53	52.75
(220)	67.78	66.65	66.49
(311)	81.71	80.12	79.92
(222)	86.02	84.75	84.10

Overall reaction: $N_2H_4 + O_2 \rightarrow N_2 + 2H_2O$(3)

Scientific studies are carried out on the development of many different electrocatalysts to improve performance in fuel cells [25]. Bimetallic or trimetallic electrocatalysts synthesized by combining different metals exhibit better catalytic activity and stability than their monometallic forms due to the synergistic effect between them [26-29]. Liang et al. synthesized Ni/C, Co/C, NiCo/C, and NiCoP/C electrocatalysts for hydrazine electrooxidation. They reported that the NiCoP/C trimetallic catalyst has greater current density, good stability, high activity, and long-term durability than other catalysts [30]. The bimetallic Cu-Ni anode catalyst was used by Filanovsky et al. for hydrazine electrooxidation. They obtained a fuel cell with high catalytic activity that can operate for a long timewith the developed anode catalyst [31]. Asset et al. investigated the hydrazine electrooxidation performance of carbon supported NiMo catalysts (NiMo/C) synthesized at different molar rates. They emphasized that the carbon-supported NiMo (9:1)/C catalyst had the highest activity. It has been reported that the catalyst with a high molybdenum ratio stabilize the N-N bond and prevent ammonia production [32]. Zabielaite et al. developed Co_{fiber}/Cu and $PtCo_{fiber}$/Cu catalyst as electrocatalyst and investigated electrochemical behavior of the synthesized catalysts. They concluded that the coating of Pt particles on Co_{fiber}/Cu increases the electrocatalytic activity [33]. Similar studies in the literature of hydrazine electrooxidation are presented in Table 1.

In this study, carbon nanotube supported monometallic (Pd), trimetallic (PdAgCo), and multimetallic (Ga@PdAgCo) catalysts with various loading ratios of Ga were developed. The hydrazine electrooxidation capacities of the catalysts synthesized by the $NaBH_4$ reduction method were determined by cyclic voltammetry (CV), chronoamperometry (CA), and impedance spectroscopy (EIS) measurements in 1 M KOH + 0.5 M N_2H_4 solution. The physical properties and surface chemistry of the catalysts were investigated by advanced characterization methods such as transmission electron microscopy (TEM), X-ray photoelectron spectroscopy (XPS), inductively coupled plasma-mass spectrometry (ICP-MS), and X-ray diffraction (XRD).

2. Experimental

2.1. Synthesis of catalyts

10% Pd/CNT, 10% Ga/CNT, and 10% PdAgCo(80:10:10)/CNT catalysts were synthesized by the $NaBH_4$ co-reduction method. The monometallic catalysts were loaded as 10% by weight of the support material, and ternary catalyst was also prepared considering a 80:10:10 metal ratio. After the precursor metal salts (K_2PdCI_4, $AgNO_3$, and $CoCl_2{\cdot}6H_2O$) were dissolved in pure water for preparation of monometallic and ternary metallic catalysts, CNT was added. The mixture was stirred in an ultrasonic bath for two hours. $NaBH_4$ was used for metal reduction. $NaBH_4$ was added dropwise to the mixture, and then it was stirred for another hour. Finally, the mixture was washed with pure water, filtered, and dried in an oven at 85 °C. The multimetallic catalysts (0.5–10% Ga@PdAgCo(80:10:10)/CNT), were prepared via $NaBH_4$ sequential reduction method. First, a suitable amount $GaCl_3$ precursor metal salt was dissolved in water, and then the synthesized PdAgCo (80:10:10)/CNT catalyst was added in the solution. Then, the experimental steps described in the co-reduction method were carried out.

2.2. Characterization of catalysts

TEM (Zeiss Sigma 300) was applied to describe surface metal distribution and particle size of the catalyst. XPS (Specs-Flex) analysis was used to determine the oxidation state of the metals. The atomic molar ratios of the catalyst were defined by ICP-MS (Agilent 7800). The crystallographic properties of the catalyst were determined by XRD (Panalytical Empyrean).

2.3. Electrochemical measurements

CV, EIS, and CA electrochemical measurements were performed in CHI 660C potentiostat device with three-electrode system such as counter electrode (platinum wire), reference electrode (Ag/AgCl), and working electrode. While preparing the working electrode (glassy carbon electrode), first catalyst ink was prepared by dissolving 3 mg of

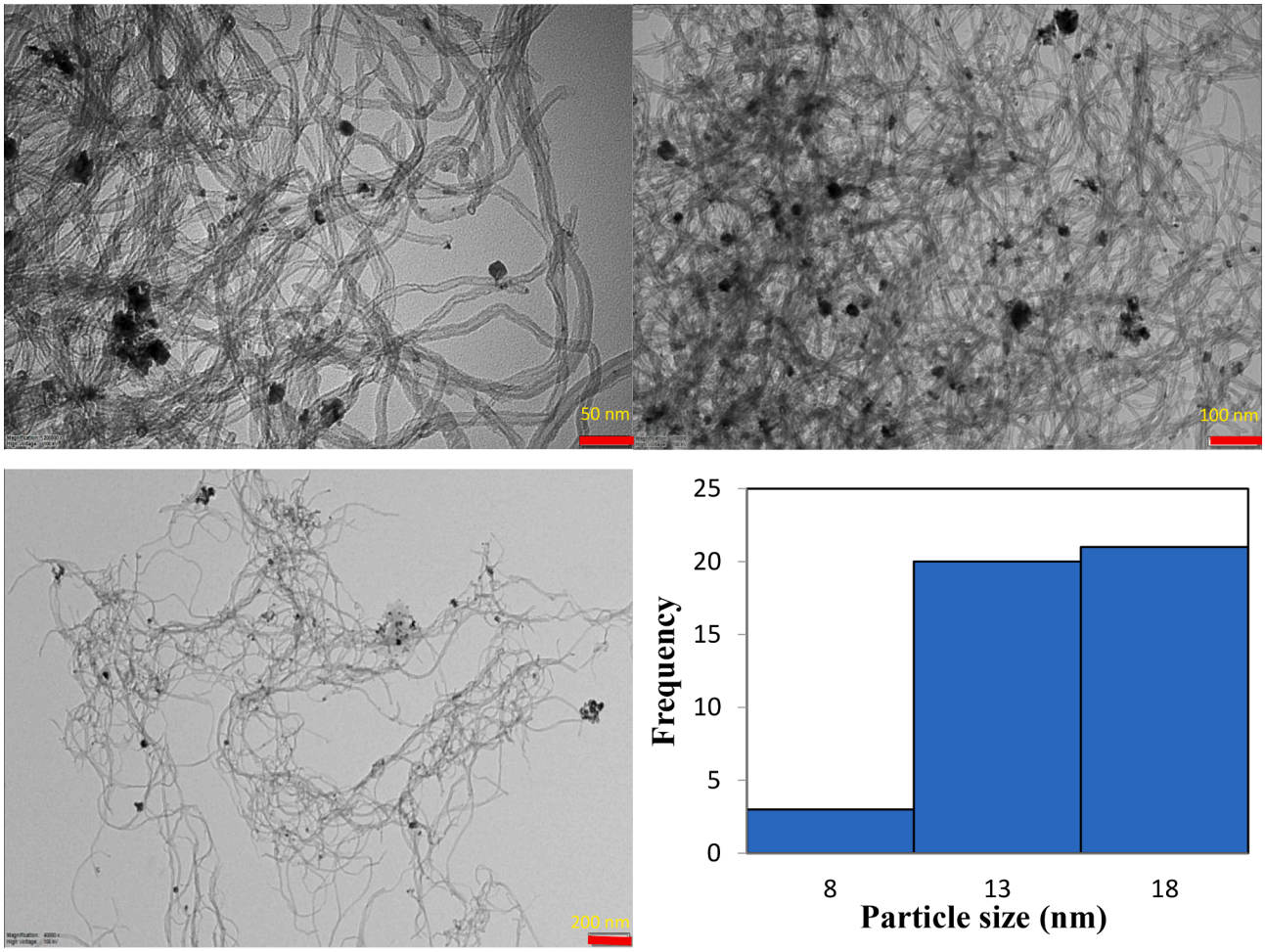

Fig. 2. TEM images and particle size histogram with related particle size distributions of 3% Ga@PdAgCo(80–10-10)/CNT catalyst at 50 nm, 100 nm, 200 nm, and 200 nm particle size histogram (related particle size distribution).

catalyst with 1 mL of 5% Nafion solution in an ultrasonic water bath. 3 μL of catalyst ink was dropped on the working electrode polished with alumina and dried at room temperature. CV measurements were applied to determine hydrazine electrooxidation activities in 1 M KOH + 0.5 M N_2H_4 solution in the range of −0.8–0.8 V. The stability of the catalyst was determined by taking CA measurements at different potentials in the range of −0.2–0.4 V. EIS measurements were carried out at −0.2, 0.2, and 0.4 V potential values in 300 kHz–0.04 Hz frequency.

3. Results and discussion

3.1. Physical characterization

The crystal structure of 10% Pd/CNT, 10% PdAgCo(80–10-10)/CNT, and 3% Ga@PdAgCo(80:10:10)/CNT catalyst was examined by XRD analysis, as demonstrated in Fig. 1. The diffraction peak of the (002) plane was obtained at about 25.7° related to the hexagonal structure of carbon. It could be observed from Fig. 1 that the XRD pattern of catalyst exhibited diffraction peaks at 39.40°, 45.60°, 66.49°, 79.92°, and 84.10°, corresponding to the (111), (200), (220), (311), and (222) planes of the Pd face-centered cubic (fcc) structure (JCPDS card no: 46–1043). In addition, PdO (110) and PdO (122) peaks were observed at 42.70° and 52.75° values [42]. Silver nanoparticles have peaks corresponding to the fcc structure, as in Pd nanoparticles [43]. There are no diffraction peaks of Co and Ga metals. Cobalt can consist of a metastable fcc phase and/or a hexagonal close-packed (hcp) phase [44]. Table 2 shows the diffraction peaks at 2θ of 10% Pd/CNT, 10% PdAgCo(80–10-10)/CNT, and 3% Ga@PdAgCo(80:10:10)/CNT catalysts It could be seen from Table 2 that negative shifts were observed in the XRD patterns with the metals added to the Pd/CNT catalyst for the PdAgCo/CNT and Ga@PdAgCo/CNT catalysts. This is due to the alloy of PdAgCo (80:10:10)/CNT and 3% Ga@PdAgCo(80:10:10)/CNT catalysts, Pd, Ag, Co, and Ga metals [45]. Ayrıca, the crystallite size of 10% Pd/CNT, 10% PdAgCo(80–10-10)/CNT, and 3% Ga@PdAgCo(80:10:10)/CNT catalysts were calculated by utilizing the Scherrer equation and found to be 9.21, 7.46, and 7.03 nm, respectively.

Figs. 2 and 3 indicates the TEM images and particle size distribution of 3% Ga@PdAgCo(80:10:10)/CNT and 7% Ga@PdAgCo(80:10:10)/CNT catalysts, respectively. It could be observed from Fig. 2 that the particles didn't form agglomeration and were generally homogeneously dispersed. However, as seen in Fig. 3, agglomeration was observed at certain parts with 7% Ga@PdAgCo(80:10:10)/CNT catalyst. The occurrence of agglomeration has a negative effect on catalytic activity. The average particle size of 3% Ga@PdAgCo(80:10:10)/CNT and 7% Ga@PdAgCo(80:10:10)/CNT catalysts was found to be 14.09 nm and 22.44 using the Image J program, respectively. According to the results of ICP-MS analysis, the molar atomic ratio of 3% Ga@PdAgCo (80:10:10)/CNT (Ga@PdAgCo(20: 67: 8: 5)) catalyst was found to be (16.0: 75.7: 0.5: 7.8) by metal order. The results of this ICP-MS analysis, ratios close to the desired metal ratios were obtained and it was observed that the metal alloy was formed.

The possible chemical states of Pd, Ag, Co, and Ga in the 3% Ga@PdAgCo(80–10-10)/CNT catalyst described by utilizing XPS analysis were given in Fig. 4(a-f). All peak positions were defined relative to

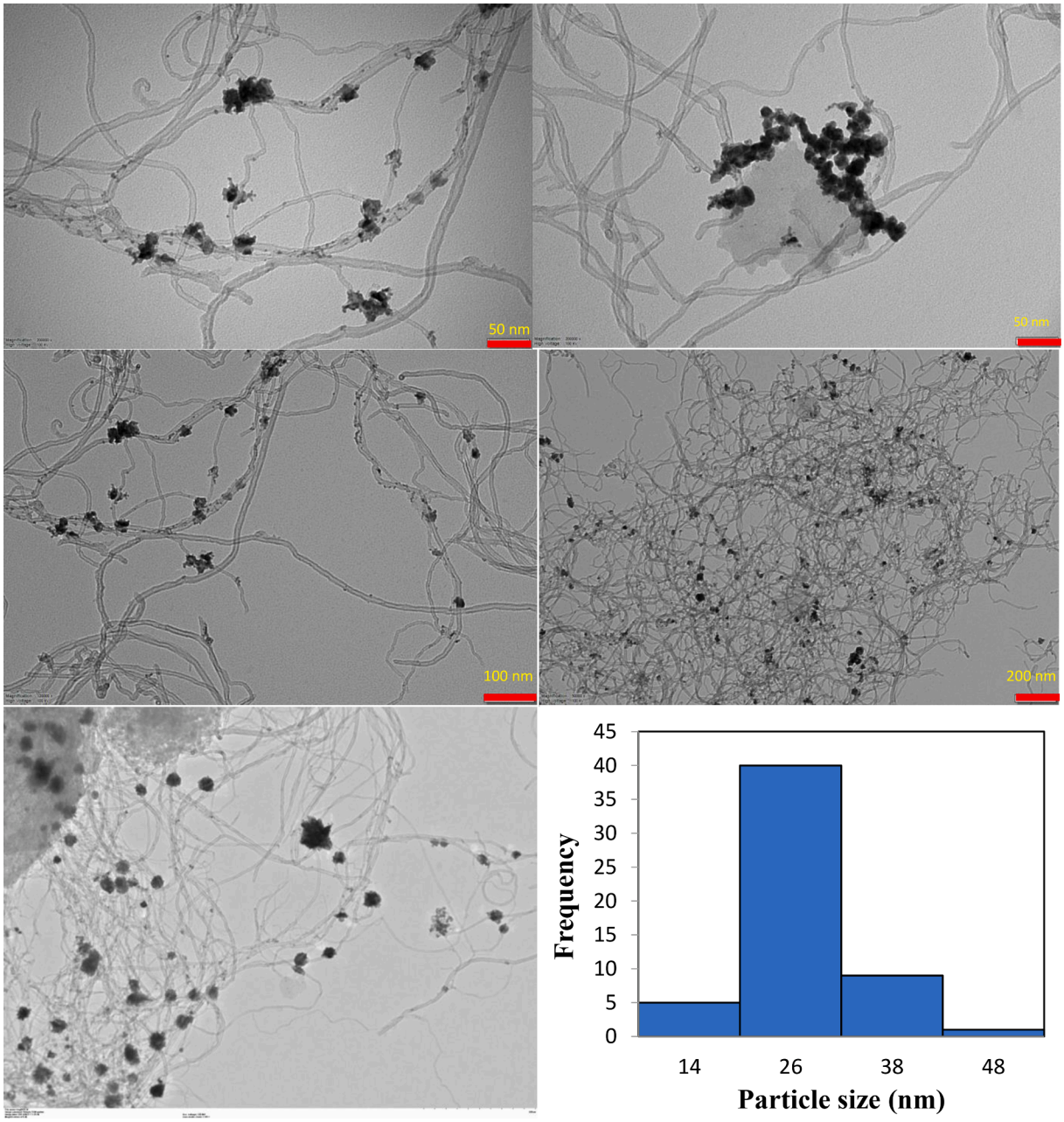

Fig. 3. TEM images and particle size histogram with related particle size distributions of 7% Ga@PdAgCo(80–10-10)/CNT catalyst at 50 nm, 100 nm, 200 nm, 500 nm, and 200 nm particle size histogram (related particle size distribution).

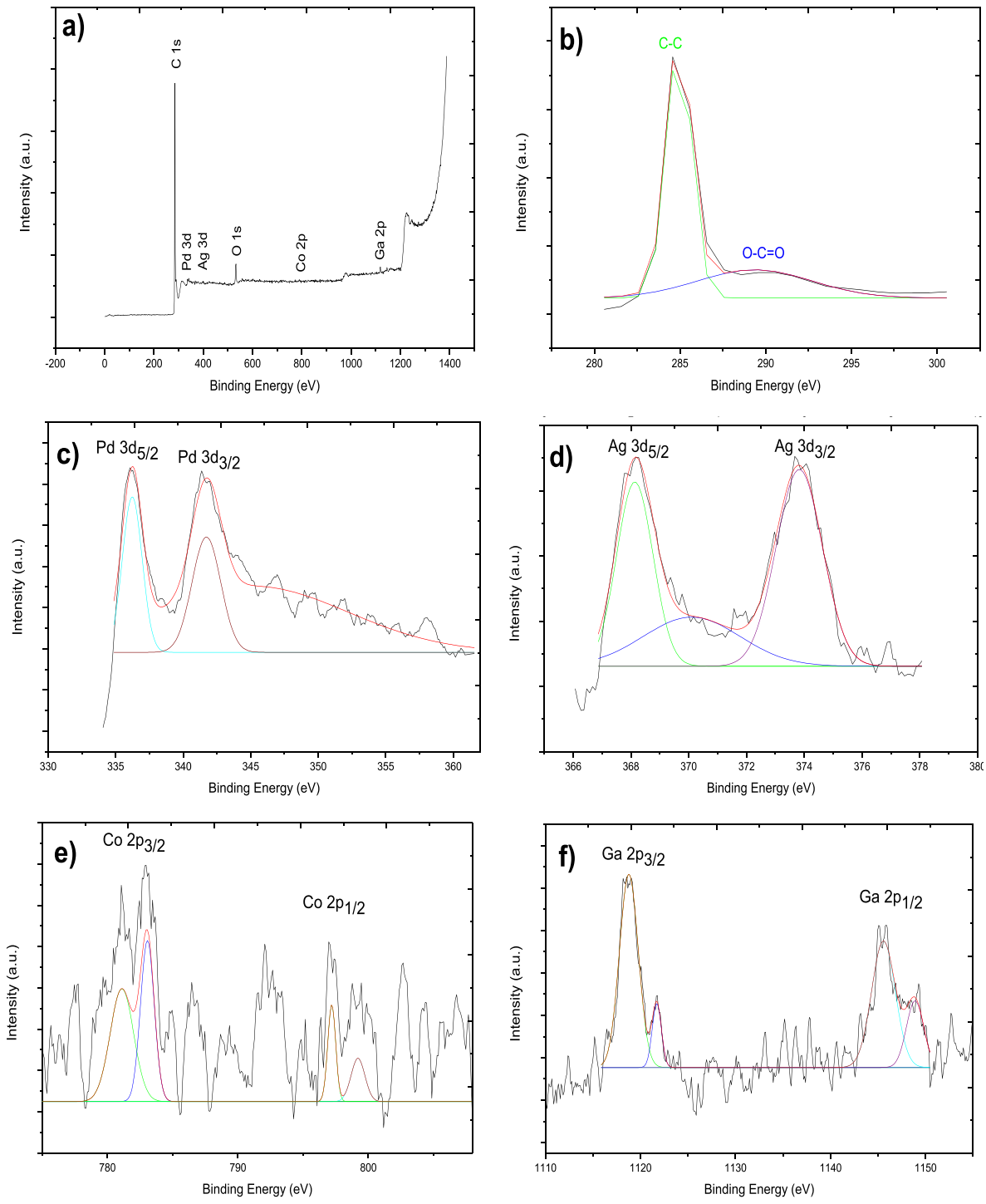

Fig. 4. XPS spectra of (a) general spectrum (b) C 1s, (c) Pd 3d, (d) Ag 3d, (e) Co 2p, (f) Ga 2p for 3% Ga@PdAgCo(80–10-10)/CNT catalyst.

Table 3
The results of curve fitting and probable chemical states of the XPS spectra of C 1s, Pd 3d, Ag 3d, Co 2p, and Ga 2p regions.

Name	Start BE	Peak BE	End BE	FWHM (eV)	Area	At. %	BE (eV)	Possible Chemical State	Relative Intensity %	Reference
C 1s	282.5	284.6	296.5	2.139	24139.2	95.048	284.6	C–C	84.64	[46]
							289.5	O-C═O	15.36	
O 1s	527.1	532.5	538.6	3.676	3217.3	4.324	–	–	–	
Pd $3d_{5/2}$	334.8	336.2	346.2	2.056	429.8	0.179	336.2	Pd^0	50.67	[47]
							341.8	Pd^0	49.33	
							368.2	Ag^+	33.63	
Ag $3d_{5/2}$	366.9	368.2	376.4	4.309	464.7	0.171	370.3	Ag^0	32.64	[48]
							373.9	Ag^+	33.73	
							781.2	Co^{3+}	25.04	
Co $2p_{3/2}$	778.4	783.0	581.2	4.195	330.2	0.103	783.0	Co^{2+}	25.27	[49,50]
							797.2	Co^{3+}	24.97	
							799.2	Co^{2+}	24.72	
							1118.8	Ga^{3+}	26.30	
Ga $2p_{3/2}$	1116.1	1118.8	1150.5	2.971	953.8	0.175	1121.7	Ga_2O_3	24.31	[51]
							1145.6	Ga^{3+}	25.20	
							1148.8	Ga_2O_3	24.19	

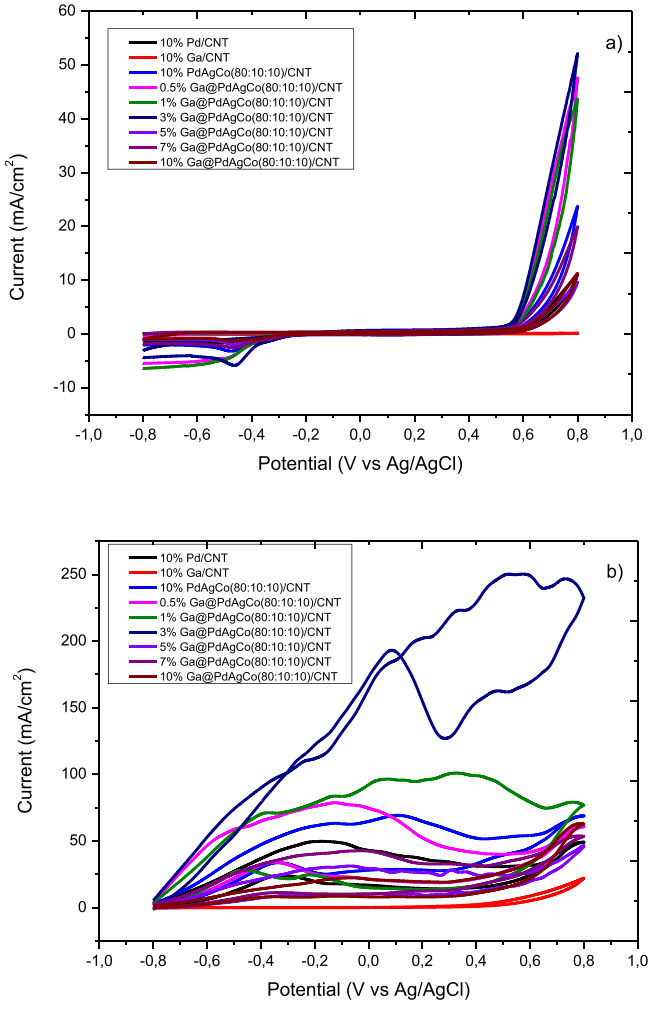

Fig. 5. Cyclic voltammograms of catalysts a) in 1 M KOH, b) 1 M in KOH + 0.5 M N_2H_4.

C 1s at a binding energy of 284.6 eV. The general spectrum of XPS analysis (Fig. 4a) of 3% Ga@PdAgCo(80–10-10)/CNT catalyst demonstrates peaks C 1s, O 1s, Pd 3d, Ag 3d, Co 2p, and Ga 2p. The C 1s of two different chemical shifts components with the binding energy of 284.6 and 289.5 eV could be assigned to C–C and O–C═O bonding [46]. The XPS spectrum of Pd 3d (Fig. 4c) openly illustrated two different peaks. The main peaks at 336.2 and 341.8 eV were attributed at $3d_{5/2}$ and $3d_{3/2}$, which indicates the possible formation of Pd^0 [47]. The binding energies at 368.2 eV and 373.9 eV of Ag 3d have two peaks at $3d_{5/2}$ and $3d_{3/2}$, corresponding silver oxide (Ag^+) (Fig. 4d). Furthermore, binding energy at 370.3 eV was attributed to the metallic silver [48]. The two characteristic important peaks of Co_3O_4 with a binding energy of 781.2 eV and 797.2 eV correlated to Co $2p_{3/2}$ and Co $2p_{1/2}$ show the existence of Co^{+2} and Co^{+3}, as illustrated in Fig. 4e. The binding energies of Co 2p could be deconvoluted into four peaks at 781.2 eV, 783.0 eV, 797.2 eV, and 799.2 eV which were attributed to Co^{3+} ($2p_{3/2}$), Co^{2+} ($2p_{3/2}$), Co^{3+} ($2p_{1/2}$), and Co^{2+} ($2p_{1/2}$) configurations, respectively [49,50]. The basis peaks of Ga 2p were located at 1118.8 eV and 1145.6 eV for $2p_{3/2}$ and $2p_{1/2}$, corresponding to Ga^{3+}, respectively. The binding energies at 1121.7 eV and 1148.8 eV can be attributed to Ga_2O_3, which is thought to be formed during synthesis [51]. In addition, the probable chemical states and curve fitting of C 1s, Pd 3d, Ag 3d, Co 2p, and Ga 2p for the 3% Ga@PdAgCo(80–10-10)/CNT catalyst were summarized in Table 3. It was observed that the metals desired to be obtained in the catalyst structure were formed as in the ICP-MS analysis result.

3.2. Electrochemical results

CV measurements were performed for hydrazine electrooxidation activities of 10% Pd/CNT, 10% PdAgCo(80:10:10)/CNT, and 0.5–10% Ga@PdAgCo(80:10:10)/CNT catalysts in 1 M KOH + 0.5 M N_2H_4 solution at a scanning rate of 50 mV/s. The CV voltagrams acquired in the −0.8–0.8 V potential range are shown in Fig. 5. OH^- adsorption/desorption peaks in the range of −0.2 to 0.6 V were observed for all catalysts. These peaks detected in the forward scan are due to hydrazine oxidation. The specific activities and peak potentials of the 10% Pd/CNT and 10% PdAgCo(80:10:10)/CNT catalysts were 49.71 mA/cm^2 (−0.17 V) and 69.11 mA/cm^2 (0.11 V), respectively (Table 4). When Ga loading increased from 0.5% to 3%, the specific activity also increased from 78.82 mA/cm^2 to 250.39 mA/cm^2. Table 4 summarizes the catalytic activities and electrochemical surface area (ECSA) values of the catalysts. By integrating the coulombic charge for the reduction of metal (Pd,

Table 4
The electrochemical behaviors of catalysts for hydrazine electrooxidation.

Catalyst	Specific Activity, mA/cm^2	Mass Activity, mA/mg Pd	Peak Potential, V	Onset Potential, V	ECSA (m^2/g)
10% Pd/CNT	49.71	4293.41	−0.17	−0.79	544.98
10% Ga/CNT	21.93	1893.66	0.80	0.80	24.65
10% PdAgCo(80:10:10)/CNT	69.11	6072.91	0.11	−0.79	1096.77
0.5% Ga@PdAgCo(80:10:10)/CNT	78.82	6960.79	−0.12	−0.79	937.77
1% Ga@PdAgCo(80:10:10)/CNT	101.17	8968.21	0.33	−0.79	1061.11
3% Ga@PdAgCo(80:10:10)/CNT	250.39	22592.66	0.52	−0.79	1392.43
5% Ga@PdAgCo(80:10:10)/CNT	31.37	2882.04	−0.07	−0.77	788.34
7% Ga@PdAgCo(80:10:10)/CNT	42.54	3975.46	−0.04	−0.76	859.22
10% Ga@PdAgCo(80:10:10)/CNT	22.36	2140.56	−0.08	−0.74	490.32

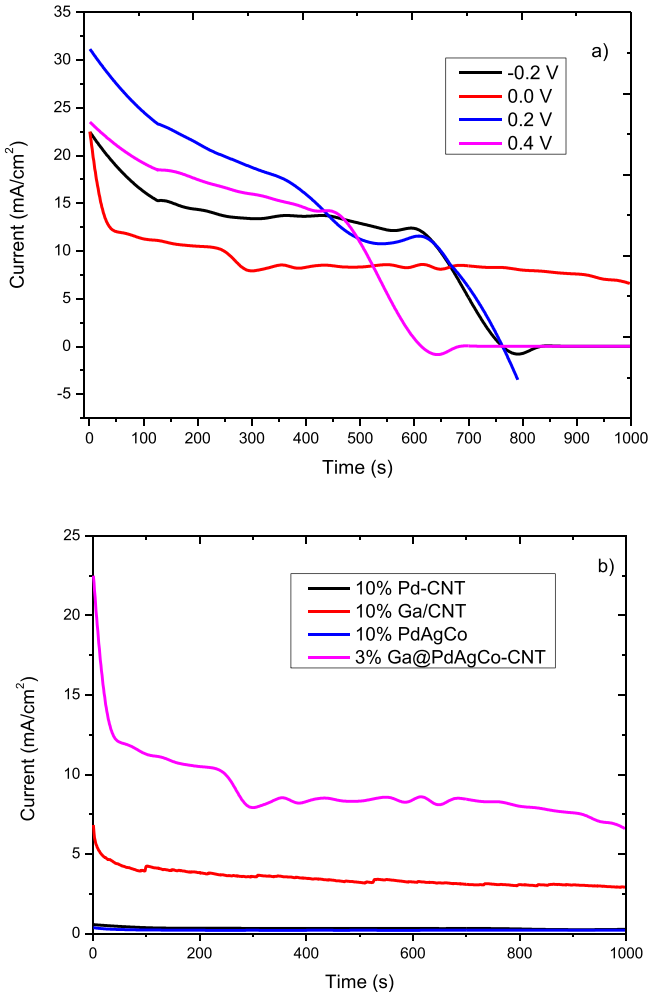

Fig. 6. Chronoamperometry curves of a) 3% Ga@PdAgCo(80:10:10)/CNT at different potentials b) comparison with other catalysts at 0.0 V.

Ag, Co, Ga) oxide in CV analyses, the ECSA values of catalysts are obtained in a 1 M KOH solution [52]. The calculation of ECSA values has been demonstrated in previous studies [5,53]. It could be observed from Table 4 that the ECSA value (1392.43 m^2/g) of 3% Ga@PdAgCo (80:10:10)/CNT catalyst was much bigger than other catalysts. Furthermore, 3% Ga@PdAgCo(80:10:10)/CNT catalyst exhibited the highest specific activity as 250.39 mA/cm^2 (22592.66 mA/mg Pd) at 0.52 V peak potential and −0.79 V onset potential. This high specific activity is explained by the synergistic effect between Ga, Pd, Ag, and Co metals. The reduction in specific activity at 5% and more Ga loadings may be due to agglomeration of Ga particles.

CA analysis was used to determine the stability of the catalysts. The CA results of 3% Ga@PdAgCo(80:10:10)/CNT catalyst in 1000 s at different potentials (0.2, 0.0, 0.2, and 0.4 V) are presented in Fig. 6a. After 1000 s, 3% Ga@PdAgCo(80:10:10)/CNT catalyst at 0.0 V potential had best stability with specific activity of 6.66 mA/cm^2. Fig. 6b shows comparison results of 3% Ga@PdAgCo(80:10:10)/CNT with 10% Pd/CNT and 10% PdAgCo(80:10:10)/CNT at 0.0 V. As seen in Fig. 6b, the 3% Ga@PdAgCo(80:10:10)/CNT catalyst had better stability at higher current than the other catalysts. The electrocatalytic resistance of the catalysts to hydrazine electrooxidation was determined by EIS measurements. Fig. 7 includes the Nyguist plots obtained at potential values of the catalysts at −0.2, 0.2, and 0.4 V. In Nyguist plots, which are known to be semicircular, the smaller the diameter of the semicircle, the lower the load transfer resistance (R_{ct}) [54]. Electron transfer between electrolyte and electrode is faster at smaller semicircular diameters [55]. Since low charge transfer resistance indicates high electrocatalytic activity, 3% Ga@PdAgCo(80:10:10)/CNT catalyst exhibited the best catalytic activity with the lowest diameter at each potential.

4. Conclusion

In this study, 10% Pd/CNT, 10% PdAgCo/CNT, and 0.5–10% Ga@PdAgCo/CNT catalysts were synthesized and hydrazine electrooxidation activities were investigated. Advance characterization techniques as TEM, XRD, XPS, and ICP-MS were applied for the characterization of catalysts. According to the TEM results of 3% Ga@PdAgCo/CNT, it was concluded that the particles were homogeneously dispersed on the carbon nanotube. However, as seen in the 7% Ga@PdAgCo/CNT catalyst, agglomeration was observed when the Ga metal was added in excess atomic ratio. The crystal size of this catalyst was calculated as 7.03 nm by XRD analysis. In addition, negative shifts were observed when metal was added in the diffraction peaks indicating alloy formation. According to the results of electrochemical measurements such as CV, CA, and EIS, 3% Ga@PdAgCo/CNT catalyst showed the best stability, lowest resistance, and highest electrocatalytic activity (250.39 mA/cm^2 and 22592.66 mA/mg Pd). The high activity was explained by the synergistic effect between metals in multi-metal particles. This result also could be attributed to the electronic state change of catalysts by the addition of Ag, Co, and Ga metals to Pd/CNT. ECSA value (1392.43 m^2/g) of the catalysts calculated from the reduction peak of the metal oxide was bigger for 3% Ga@PdAgCo/CNT compared to other catalysts. The reason for showing the highest catalytic activity of the 3% Ga@PdAgCo/CNT catalyst is that it agglomerates when more Ga metal is added. Ga@PdAgCo/CNT catalyst is a promising anode catalyst for DHFCs with its high specific and mass activity values.

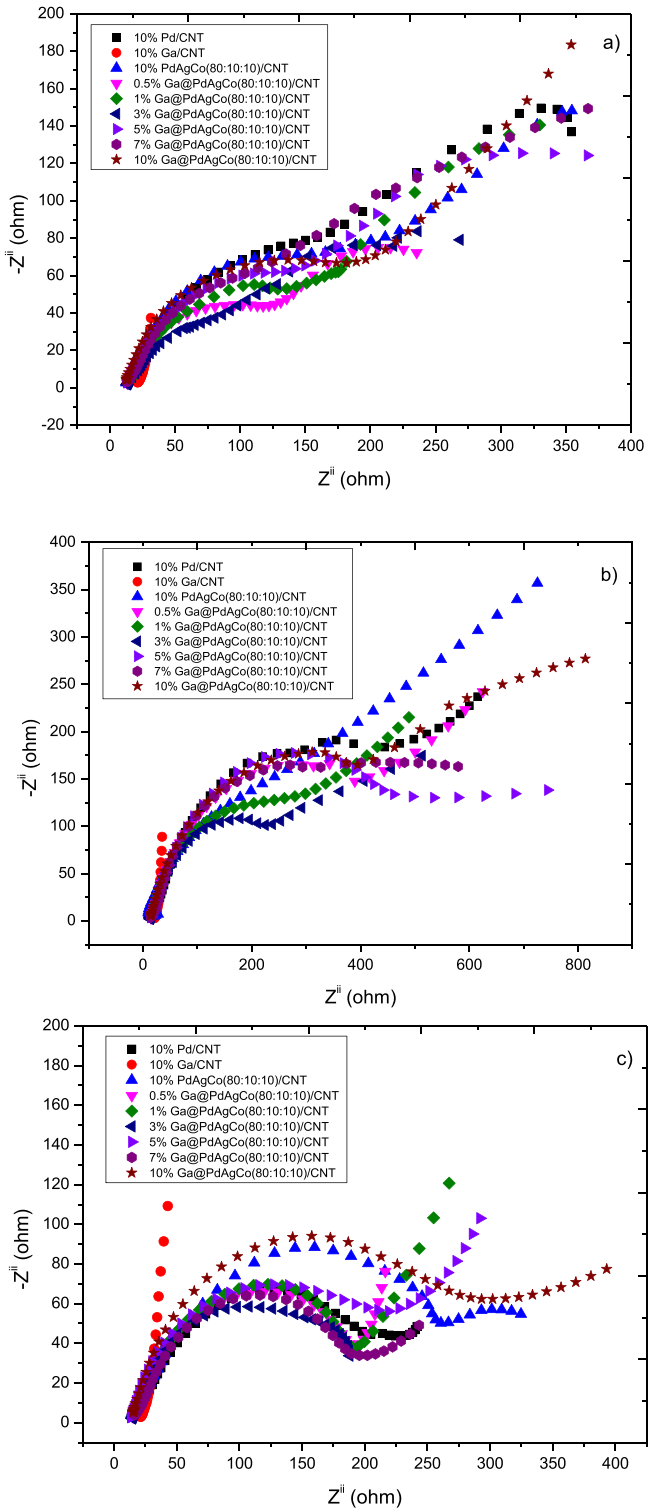

Fig. 7. Nyguist plots of catalysts at a) −0.2 V, b) 0.2 V, c) 0.4 V.

CRediT authorship contribution statement

Sefika Kaya: Writing – original draft, Writing – review & editing. **Aykut Caglar:** Writing – original draft, Writing – review & editing. **Hilal Kivrak:** Writing – original draft, Writing – review & editing, Conceptualization, Supervision.

Declaration of Competing Interest

The authors declare that they have no known competing financial interests or personal relationships that could have appeared to influence the work reported in this paper.

References

[1] Daas BM, Ghosh S. Fuel cell applications of chemically synthesized zeolite modified electrode (ZME) as catalyst for alcohol electro-oxidation - A review. J Electroanal Chem 2016;783:308–15.

[2] Cheng J, He GH, Zhang FX. A mini-review on anion exchange membranes for fuel cell applications: Stability issue and addressing strategies. Int J Hydrogen Energy 2015;40(23):7348–60.

[3] Thiam HS, Daud WRW, Kamarudin SK, Mohammad AB, Kadhum AAH, Loh KS, et al. Overview on nanostructured membrane in fuel cell applications. Int J Hydrogen Energy 2011;36(4):3187–205.

[4] Armeanu DS, Gherghina SC, Pasmangiu G. Exploring the causal nexus between energy consumption, environmental pollution and economic growth: empirical evidence from central and Eastern Europe. Energies 2019;12(19).

[5] Caglar A, Cogenli MS, Yurtcan AB, Alal O, Kivrak H. Remarkable activity of a ZnPdPt anode catalyst: Synthesis, characterization, and formic acid fuel cell performance. J Phys Chem Solids 2021;156:110163.

[6] Faruk Er O, Ulas B, Ozok O, Kivrak A, Kivrak H. Design of 2-(4-(2-pentyllbenzo b thiophen-3-yl)benzylidene)malononitrile based remarkable organic catalyst towards hydrazine electrooxidation. J Electroanal Chem 2021;888:115218.

[7] Wang Y, Chen KS, Mishler J, Cho SC, Adroher XC. A review of polymer electrolyte membrane fuel cells: technology, applications, and needs on fundamental research. Appl Energy 2011;88(4):981–1007.

[8] Eid K, Wang H, Malgras V, Alshehri SM, Ahamad T, Yamauchi Y, et al. One-step solution-phase synthesis of bimetallic PtCo nanodendrites with high electrocatalytic activity for oxygen reduction reaction. J Electroanal Chem 2016; 779:250–5.

[9] de Oliveira DC, Silva WO, Chatenet M, Lima FHB. NiOX-Pt/C nanocomposites: Highly active electrocatalysts for the electrochemical oxidation of hydrazine. Appl Catal B-Environ 2017;201:22–8.

[10] Bae S, Park J, Hwang Y, Park JS, Lee J, Jeong B. Steam activation of Fe-N-C catalyst for advanced power performance of alkaline hydrazine fuel cells. J Energy Chem 2022;64:276–85.

[11] Yadav M, Xu Q. Liquid-phase chemical hydrogen storage materials. Energy Environ Sci 2012;5(12):9698–725.

[12] Granot E, Filanovsky B, Presman I, Kuras I, Patolsky F. Hydrazine/air direct-liquid fuel cell based on nanostructured copper anodes. J Power Sources 2012;204: 116–21.

[13] Crisafulli R, de Barros VVS, Rodrigues de Oliveira FE, de Araújo Rocha T, Zignani S, Spadaro L, et al. On the promotional effect of Cu on Pt for hydrazine electrooxidation in alkaline medium. Appl Catal B-Environ 2018;236:36–44.

[14] Kang W, Guo H, Varma A. Noble-metal-free NiCu/CeO2 catalysts for H-2 generation from hydrous hydrazine. Appl Catal B-Environ 2019;249:54–62.

[15] Wen He, Cao G-X, Chen M-H, Qiu Y-P, Gan L-Y, Wang P. Surface phosphorization of hierarchically nanostructured nickel molybdenum oxide derived electrocatalyst for direct hydrazine fuel cell. Appl Catal B 2020;268:118388.

[16] Yamada K, Asazawa K, Yasuda K, Ioroi T, Tanaka H, Miyazaki Y, et al. Investigation of PEM type direct hydrazine fuel cell. J Power Sources 2003;115(2):236–42.

[17] Deng J, Li X, Imhanria S, Chen K, Deng X, Wang W. Molybdenum carbide-nitrogen doped carbon composites as effective non-precious electrocatalyst for direct hydrazine fuel cell. Electrochim Acta 2021;384:138417.

[18] Hwang H, Hong S, Kim D-H, Kang M-S, Park J-S, Uhm S, et al. Optimistic performance of carbon-free hydrazine fuel cells based on controlled electrode structure and water management. Journal of Energy Chemistry 2020;51:175–81.

[19] Xue Qi, Huang H, Zhu J-Y, Zhao Y, Li F-M, Chen P, et al. Au@Rh core-shell nanowires for hydrazine electrooxidation. Appl Catal B 2020;278:119269.

[20] Serov A, Kwak C. Direct hydrazine fuel cells: A review. Appl Catal B-Environ 2010; 98(1–2):1–9.

[21] Firdous N, Janjua NK. CoPtx/gamma-Al2O3 bimetallic nanoalloys as promising catalysts for hydrazine electrooxidation. Heliyon 2019;5(3).

[22] Wu LS, Dai HB, Wen XP, Wang P. Ni-Zn Alloy Nanosheets Arrayed on Nickel Foamas a Promising Catalyst for Electrooxidation of Hydrazine. Chemelectrochem 2017;4(8):1944–9.

[23] Yi Q, Chu H, Tang M, Zhang Y, Liu X, Zhou Z, et al. A novel membraneless direct hydrazine/air fuel cell. Fuel Cells 2014;14(6):827–33.

[24] Wen H, Gan L-Y, Dai H-B, Wen X-P, Wu L-S, Wu H, et al. In situ grown Ni phosphide nanowire array on Ni foam as a high-performance catalyst for hydrazine electrooxidation. Appl Catal B-Environ 2019;241:292–8.

[25] Ulas B, Caglar A, Kivrak A, Kivrak H. Atomic molar ratio optimization of carbon nanotube supported PdAuCo catalysts for ethylene glycol and methanol electrooxidation in alkaline media. Chem Pap 2019;73(2):425–34.

[26] Hu SZ, Munoz F, Noborikawa J, Haan J, Scudiero L, Ha S. Carbon supported Pd-based bimetallic and trimetallic catalyst for formic acid electrochemical oxidation. Appl Catal B-Environ 2016;180:758–65.

[27] Liu C, Cai X, Wang J, Liu J, Riese A, Chen Z, et al. One-step synthesis of AuPd alloy nanoparticles on graphene as a stable catalyst for ethanol electro-oxidation. Int J Hydrogen Energy 2016;41(31):13476–84.

[28] Shen SY, Zhao TS, Xu JB, Li YS. Synthesis of PdNi catalysts for the oxidation of ethanol in alkaline direct ethanol fuel cells. J Power Sources 2010;195(4):1001–6.
[29] Kivrak H, Atbas D, Alal O, Çögenli MS, Bayrakceken A, Mert SO, et al. A complementary study on novel PdAuCo catalysts: Synthesis, characterization, direct formic acid fuel cell application, and exergy analysis. Int J Hydrogen Energy 2018;43(48):21886–98.
[30] Liang B, Wang Y, Liu X, Tan T, Zhang L, Wang W. Nickel-cobalt alloy doping phosphorus as advanced electrocatalyst for hydrazine oxidation. J Alloy Compd 2019;807:151648.
[31] Filanovsky B, Granot E, Presman I, Kuras I, Patolsky F. Long-term room-temperature hydrazine/air fuel cells based on low-cost nanotextured Cu-Ni catalysts. J Power Sources 2014;246:423–9.
[32] Asset T, Roy A, Sakamoto T, Padilla M, Matanovic I, Artyushkova K, et al. Highly active and selective nickel molybdenum catalysts for direct hydrazine fuel cell. Electrochim Acta 2016;215:420–6.
[33] Zabielaite A, Balciunaite A, Simkunaite D, Lichusina S, Stalnioniene I, Simkunaite-Stanyniene B, et al. High performance direct N2H4-H2O2 fuel cell using fiber-shaped co decorated with Pt crystallites as anode electrocatalysts. J Electrochem Soc 2019;167(1).
[34] Akbar K, Kim JH, Lee Z, Kim M, Yi Y, Chun S-H. Superaerophobic graphene nano-hills for direct hydrazine fuel cells. NPG Asia Mater 2017;9(5):e378–.
[35] Chen LX, Jiang LY, Wang AJ, Chen QY, Feng JJ. Simple synthesis of bimetallic AuPd dendritic alloyed nanocrystals with enhanced electrocatalytic performance for hydrazine oxidation reaction. Electrochim Acta 2016;190:872–8.
[36] Ding J, Kannan P, Wang P, Ji S, Wang H, Liu Q, et al. Synthesis of nitrogen-doped MnO/carbon network as an advanced catalyst for direct hydrazine fuel cells. J Power Sources 2019;413:209–15.
[37] Rostami H, Omrani A, Rostami AA, Emamgholizadeh A. Electrooxidation of hydrazine in alkaline medium at carbon paste electrode decorated with poly(P-phenylendiamine/ZnO) nanocomposite. Ionics 2015;21(4):1073–80.
[38] Zhao A, Sun H, Chen L, Huang Y, Lu X. Development of highly efficient and scalable free-standing electrodes for the fabrication of hydrazine-O-2 fuel cell. Mater Res Express 2019;6(8):085533.
[39] Yan X, Meng F, Xie Y, Liu J, Ding Y. Direct N2H4/H2O2 fuel cells powered by nanoporous gold leaves. Sci Rep 2012;2(1).
[40] Cazetta AL, Zhang T, Silva TL, Almeida VC, Asefa T. Bone char-derived metal-free N- and S-co-doped nanoporous carbon and its efficient electrocatalytic activity for hydrazine oxidation. Appl Catal B-Environ 2018;225:30–9.
[41] Wang T, Wang Q, Wang Y, Da Y, Zhou W, Shao Y, et al. Atomically dispersed semi-metallic selenium on porous carbon membrane as an electrode for hydrazine fuel cells. Angew Chem-Int Ed 2019;58(38):13466–71.
[42] Caglar A, Cogenli MS, Yurtcan AB, Kivrak H. Effective carbon nanotube supported metal (M=Au, Ag Co, Mn, Ni, V, Zn) core Pd shell bimetallic anode catalysts for formic acid fuel cells. Renewable Energy 2020;150:78–90.
[43] Pal H, Sharma V, Kumar R, Thakur N. Facile synthesis and electrical conductivity of carbon nanotube reinforced nanosilver composite. Zeitschrift Fur Naturforschung Section a-a Journal of Physical Sciences 2012;67(12):679–84.
[44] Meng QK, Guo S, Zhao XQ, Veintemillas-Verdaguer S. Bulk metastable cobalt in fcc crystal structure. J Alloy Compd 2013;580:187–90.
[45] Ungar T. Dislocation densities, arrangements and character from X-ray diffraction experiments. Mater Sci Eng A 2001;309:14–22.
[46] Wu Y, Lin YC, Xu J. Synthesis of Ag-Ho, Ag-Sm, Ag-Zn, Ag-Cu, Ag-Cs, Ag-Zr, Ag-Er, Ag-Y and Ag-Co metal organic nanoparticles for UV-Vis-NIR wide-range bio-tissue imaging. Photochem Photobiol Sci 2019;18(5):1081–91.
[47] Thunyaratchatanon C, Luengnaruemitchai A, Jitjamnong J, Chollacoop N, Chen SY, Yoshimura Y. Influence of Alkaline and Alkaline Earth Metal Promoters on the Catalytic Performance of Pd-M/SiO2 (M = Na, Ca, or Ba) Catalysts in the Partial Hydrogenation of Soybean Oil-Derived Biodiesel for Oxidative Stability Improvement. Energy Fuels 2018;32(9):9744–55.
[48] Ambroziak R, Hołdyński M, Płociński T, Pisarek M, Kudelski A. Cubic Silver Nanoparticles Fixed on TiO2 Nanotubes as Simple and Efficient Substrates for Surface Enhanced Raman Scattering. Materials 2019;12(20):3373.
[49] Aboelazm EA, Ali GA, Chong KF. Cobalt oxide supercapacitor electrode recovered from spent lithium-ion battery. Chemistry of. Adv Mater 2018;3(4).
[50] Smyrnioti M, Ioannides T. Synthesis of cobalt-based nanomaterials from Organic Precursors. In: Maaz K, editor. Cobalt. InTech; 2017.
[51] Rodríguez CIM, Álvarez MÁL, Rivera JdJF, Arízaga GGC, Michel CR. α-Ga2O3 as a Photocatalyst in the Degradation of Malachite Green. ECS J Solid State Sci Technol 2019;8(7):Q3180.
[52] Jin L, Xu H, Chen C, Song T, Wang C, Wang Y, et al. Uniform PdCu coated Te nanowires as efficient catalysts for electrooxidation of ethylene glycol. J Colloid Interface Sci 2019;540:265–71.
[53] Caglar A, Kivrak H. Superior formic acid electrooxidation activity on carbon nanotube-supported binary Pd nanocatalysts prepared via sequential sodium borohydride reduction technique. Surf Interface Anal 2021;53(8):716–26.
[54] Hefnawy MA, Fadlallah SA, El-Sherif RM, Medany SS. Nickel-manganese double hydroxide mixed with reduced graphene oxide electrocatalyst for efficient ethylene glycol electrooxidation and hydrogen evolution reaction. Synth Met 2021;282:116959.
[55] Zhang D, Li X, Xiang Q. Triethanolamine as an efficient electrolyte additive for borohydride electrooxidation on Ni based catalyst. Mater Lett 2022;306:130922.